Chapter 5

Photoionization spectroscopy by TOF measurements

In the preceding chapter, we have discussed the present experimental results for the TCS up to the SIT I_{15} along with theoretical calculations up to the SIT I_{17} of helium. The most important physics is the observation of features caused by quantum chaos in the simplest multibody system, namely the two-electron system such as He atom. However, all these studies were performed with statistical tools, such as the NNS distribution of energy levels, the Lorentzian distribution of Fano q parameters, and the Porter-Thomas function of resonant linewidths. Since only a small fraction of the resonances can be observed experimentally, most of these statistical studies were made on the basis of theoretical results. Therefore, experimental studies of the PCSs σ_n and ADPs β_n can substantiate theoretical methods and assure the validity of these statistical analysis derived from theoretical data. In addition, since the PCSs and ADPs carry additional coupling information of the outgoing channels, quantum chaos is expected to manifest itself more easily or in different ways than in the TCSs. Vice versa, the success of the present experimental and theoretical studies on the TCSs in this highly excited region will encourage studies of PCSs and ADPs.

Due to various couplings among the outgoing channels, the PCSs, σ_n and the ADPs, β_n, are more sensitive to the quality of the wave functions and theoretical methods than the TCS, σ_T, and therefore represent the most critical assessment of the theoretical methods. Moreover, because each decay channel can be influenced in a different way, the σ_n and β_n are more sensitive to the influences of perturbers. As a result, more resonances with pronounced variations are expected in σ_n than σ_T. As an example, the resonance $8, 4_{10}$ of the secondary series is resolved in the present PCS measurements in contrast to the TCS data, although latter were measured with better resolution and signal-to-noise ratio [30].

Similarities in the variations of the PCSs and the ADPs caused by the resonances in the energy region up to the SIT I_5 were observed for the first time by Menzel *et al.* [34, 35]. These so-called 'general patterns' can be well understood by the propensity rules for autoionization based on the molecular adiabatic approximations [33] (see Sect.

5.3.3). As the photon energy increases, the structures in the PCSs get more complicated due to interferences caused by an increasing number of perturbers, and the general patterns begin to dissolve. An experimental confirmation of these theoretical predictions requires high-resolution photoemission measurements at the energies beyond the ionization threshold I_5.

In addition, in the photon energy region below the SIT I_6, the mirroring behavior in the PCSs for the double-excitation resonances has become an interesting topic in recent years since Liu and Starace developed an analytical expression for it [36]. The mirroring behavior means that the variations in the vicinity of a resonance between any two PCSs exhibit a very similar behavior. The sum of these two PCSs is the TCS. In this dissertation, we shall extend the analytical expression of Ref. [36] to a general case, which allows us to understand completely the mirroring behavior in the n-specific PCS as well as in the l-specific PCS given in last chapter of the dissertation.

Due to the reasons mentioned above, the PCSs in region of the last eV below the double-ionization threshold have drawn considerable attention both in experimental and theoretical studies. The incentive for the present work was the insight that an analysis of the propensity rules and of the mirroring behavior of PCSs as well as the ADPs of autoionizing double-excitation states in helium can provide a deep understanding of the decay dynamics of two-electron atoms. First measurements of PCSs of He had been performed by Lindle *et al.* [103]; these studies, however, were limited to excitations approaching the ionization limit I_3, due to the low photon intensities achieved at the first-generation light sources available at that time. Menzel *at al.* then reported on the measurements of PCSs and ADPs up to the SIT I_5 employing two spherical-sector-plate electrostatic analyzers [34, 35]. Czasch *et al.* [102] studied the photon energy region from the SITs I_9 to I_{16}. In the present dissertation, we extend the experimental studies of PCSs up to the SIT I_9 [37, 104] and of ADPs up to the SIT I_7, filling the gap between Menzel's measurements and the experimental results of Czasch *et al.*. The PCSs and ADPs presented in this dissertation were derived from photoemission spectra taken by a TOF electron spectrometer. The results of state-of-the-art R-matrix calculations, performed by T. Schneider and partly presented in Ref. [33], are also displayed along with the experimental results for the PCSs. Other calculations were performed by van der Hart *et al.* [63], who published their results for σ_n up to the SIT I_9. To our knowledge, no calculations and measurements are available for a comparison with the present experimental results for the ADPs above the SIT I_5.

5.1 Experimental set-up

State-of-the-art high-resolution monochromators in combination with TOF photoelectron spectrometers allow one to explore the autoionization of resonances in the highly excited region. Here, we present photoelectron emission measurements and extract the various PCSs below the SIT I_9 and the ADP below the SIT I_7 from the recorded spectra. The experiments were performed at the undulator beamline U125/2-SGM (BUS-

beamline) [50] of the Berliner Elektronenspeicherring für Synchrotronstrahlung (BESSY) using a photon energy resolution of $\Omega \cong 6$ meV (FWHM). The optical layout of the BUS beamline is displayed in Fig. 2.4, and the exit slit was set to a value of $\cong 40$ μm. A needle (10 cm long, less than 500 μm inner diameter) directs an effusive jet of gas to the interaction region; the background pressure in the chamber was $\cong 10^{-4}$ mbar. From the count rate and calculated cross sections, we estimate the pressure in the interaction region to be of the order of 10^{-2} mbar.

For the measurements of the PCS, one TOF spectrometer [22] was mounted at the magic angle, i.e. in the dipole plane at an angle of $\theta = 54.7°$ relative to the polarization direction of the incoming light. The schematics of the experimental set-up for a measurement of PCSs and a corresponding photograph from the inside of the experimental chamber is displayed in Fig. 5.1. The TOF spectrometer shown in this figure was used for the PCS measurements. For this geometry equation (1.22) reveals that the angular distribution causes no effect on the derived PCSs.

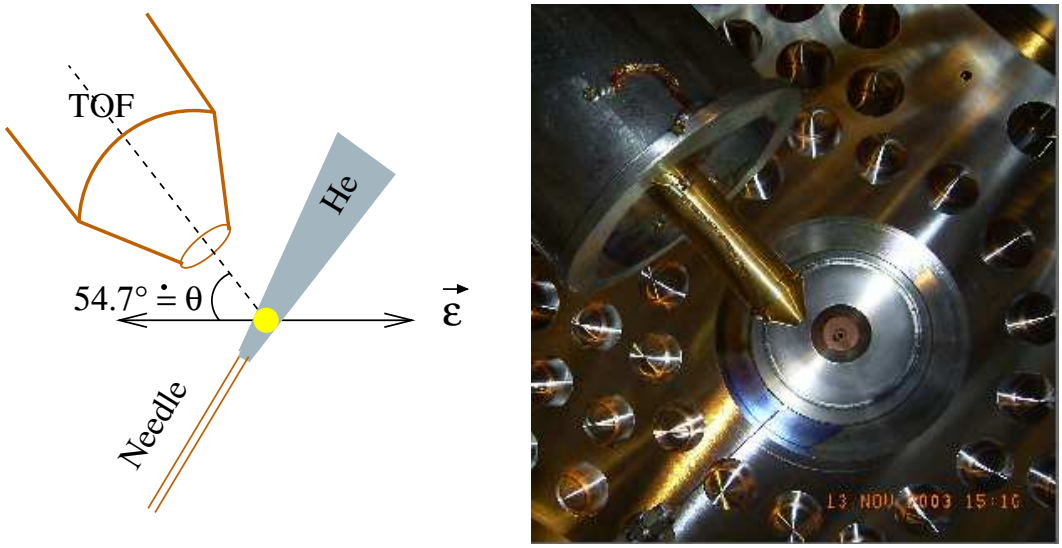

Figure 5.1: Schematics of the experimental set-up for PCS measurements and corresponding photograph from the inside of the experimental chamber. The propagation direction of the light is out of the paper plane; the polarization is horizontal as shown in the drawing on the left hand side.

Equation (1.22) contains the two parameters, σ_n and β_n. For a measurement of the β-parameters, at least two TOF detectors are needed to take differential cross sections (DCS) $d\sigma/d\Omega$. To improve the statistics and to reduce systematic errors, more analyzers can be mounted and used for taking data simultaneously. Figures 5.2 and 5.3 show photographs of the experimental ball chamber from the outside and from the inside, respectively; this chamber was used for the measurements of β-parameter below the SIT I_7. A number of TOF spectrometers [22] were mounted at various angles in the dipole plane perpendicular to the propagation of light. The TOF spectrometers mounted on the upper half of ball chamber can be seen in Figs. 5.2. The structure of these TOF

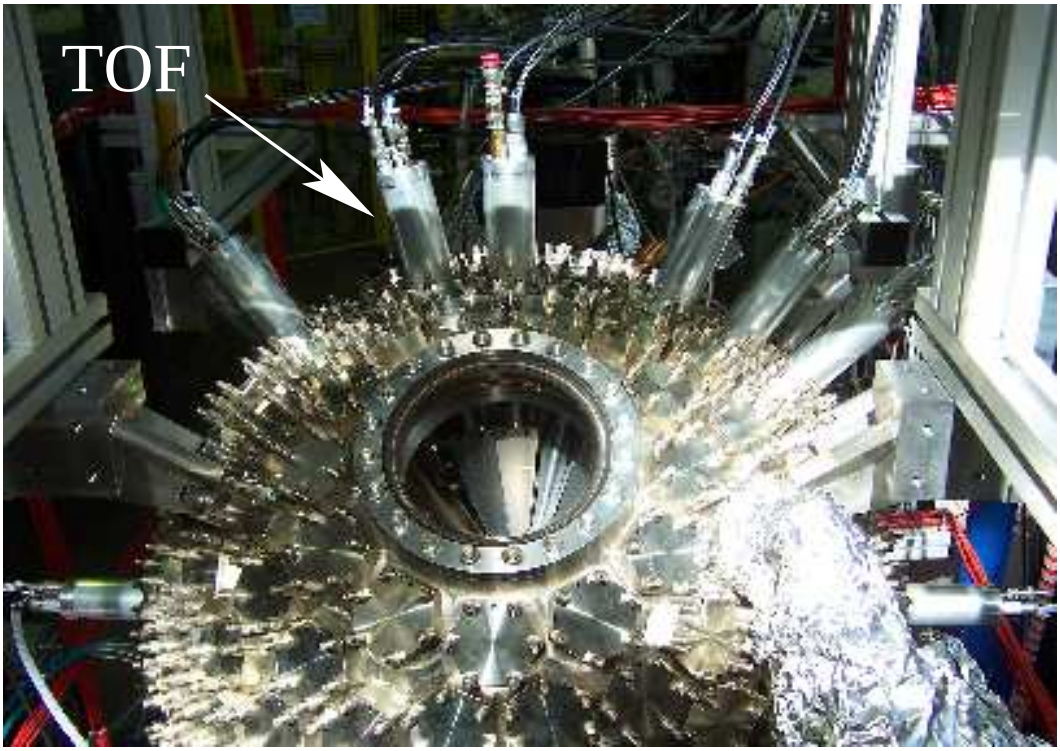

Figure 5.2: The outside of the ball-chamber for the measurements of the DCSs and ADPs. 8 TOF photoelectron spectrometers are seen in the figure.

spectrometers is identical, and the flight tube inside the chamber is about 30 cm long. A ring centered inside the chamber ensures that all TOF spectrometers are mounted at equal distances. One of the TOF spectrometers is normally mounted at the magic angle, and can be used to determine the PCSs directly.

To increase the transmission for the electrons with low kinetic energies, three accelerating voltages were applied on each TOF spectrometers, and normally their values were set individually between 1 and 3 V (see Fig. 2.7). In addition, a potential of $\cong$ 0.5 V could be applied to the needle of gas inlet in order to increase the transmission. To compensate the earth magnetic field, three pairs of Helmholtz coils were installed. This is necessary because the order of the magnetic field of the earth in the interaction region would strongly reduce the photoelectron transmission, in particular for those photoelectrons with low kinetic energy. With $\beta_2 \cong 0$ [105], the $n = 2$ satellite of the time spectrum of helium in the photon energy region directly above the SIT I_2 can be used for the adjustments of the magnetic compensation since the corresponding electrons have a very low kinetic energy and a quite high count rate. For the ADP measurements, a number of TOFs was mounted at various angles. Under this condition, the adjustment of magnetic field compensation leads normally to an increase in the transmissions of some TOF spectrometers, while for others the transmission gets worse. Therefore, after the general adjustment of magnetic fields, the relative transmission of each individual TOF

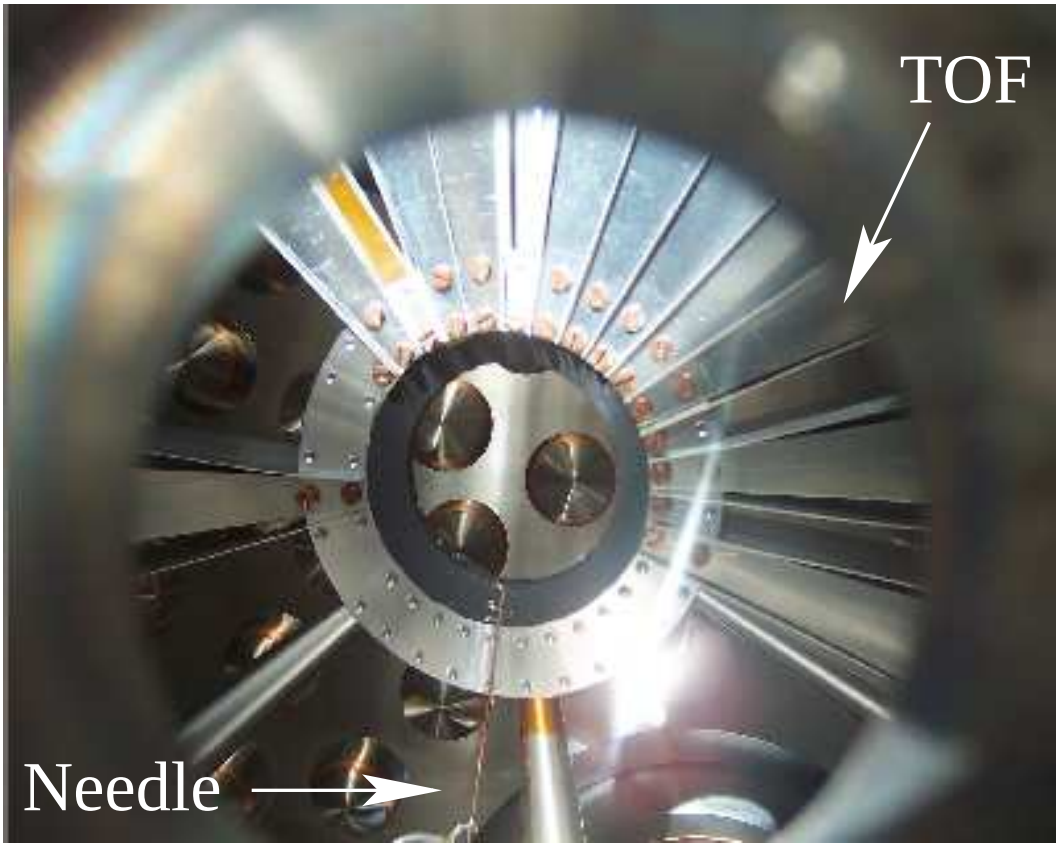

Figure 5.3: The inside of the ball-chamber with 12 TOF photoelectron spectrometers mounted.

has to be determined; this will be discussed later.

5.2 Data acquisition

In order to eliminate the influences caused by the decrease of the ring current and fluctuations of the gas pressure in the interaction region during data taking, the time spectra have to be normalized before converted into energy spectra by the time-to-energy conversion introduced in Sect. 2.4.3. Ideally, we could use the 1s-line of the various TOF spectrometers, mounted at different angles to normalize the intensities of the other satellite lines, since σ_1 can be assumed to be structureless. However, according to $\beta_{1s} = 2$, the 1s-line is absent in the 90°-TOF spectrum. Assuming that the count rates of all satellites in all TOF spectra are influenced in the same way by the photon flux and the target pressure, one can also use the intensity of the 1s-line of any TOF spectrum for normalization of the time spectrum of the 90°-spectrometer. In practice, the 1s-line of the 0°-TOF spectrometer is used for normalization because of the highest count rate. Based on theoretical results which show some weak resonances in σ_1, we can estimate that the error produced by this procedure is $\leq 10\%$ for measurements below

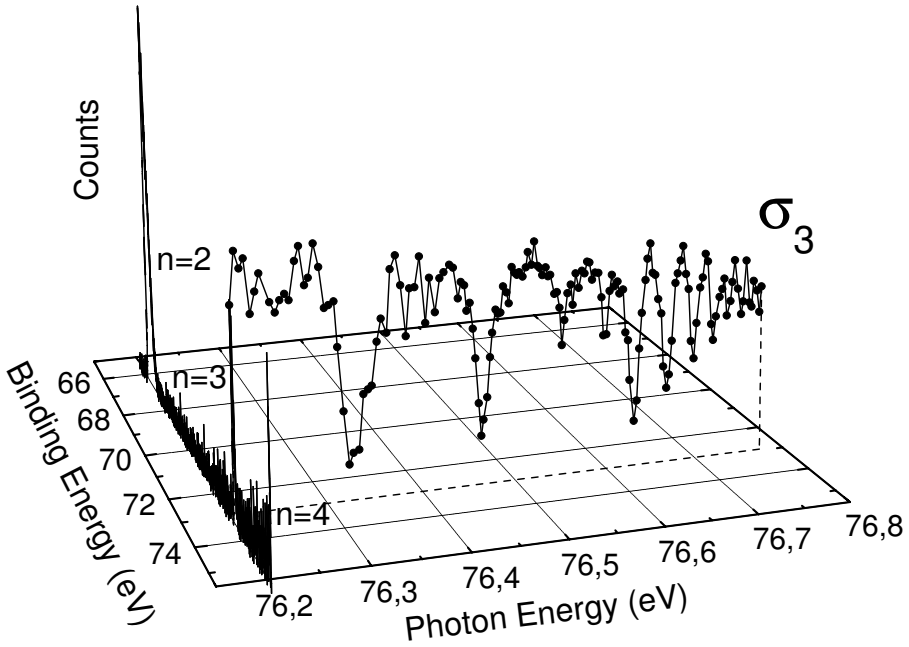

Figure 5.4: The spectrum along the binding energy axis represents an experimental photoemission spectrum recorded at $h\nu = 76.2$ eV, with the satellites $n = 2$ to 4 representing the ionic final states of $He^+(n)$. The solid curve through the data points represents the PCS σ_3 that can be derived from a large number of such photoemission spectra (not shown here) recorded at different photon energies. For details see text.

the ionization threshold I_5, $\leq 6\%$ below I_6, $\leq 7\%$ below I_7, $\leq 3\%$ below I_8, and $\leq 2\%$ below I_9.

After normalization, the second step of the data analysis procedure is to determine the efficiency factors for the different TOF spectrometer. This is particularly important for measurement of the β parameter. These efficiency factors are determined by comparing the intensities of the $1s$ line due to its high kinetic energy and the energy independence of the efficiency factor of a TOF (see Sect. 2.4.3).

As an example, an experimental photoemission spectrum (PES), taken with $h\nu = 76.2$ eV, is presented in Fig. 5.4 in form of a three-dimensional plot. From the PES, the integral intensities of the satellite peaks, i.e. $n \geq 2$, can be extracted and plotted as a function of photon energy, resulting in the PCS σ_n. As shown in Fig. 5.4 for the example of σ_3, the PCS was derived from approximately one hundred PESs, and each point in the PCS corresponds to one PES with different photon energies. Since the measuring time for one PES spectrum is of the order of 5 to 10 minutes, the data acquisition for the PCSs below one ionization threshold takes several ten hours.

5.3 Channel-resolved measurements up to I_9

In this section, we present the results of PCS measurements below the SITs I_5 to I_9 of He. General pattern and mirroring behavior in the PCSs will be the topics in this part of

the dissertation. With these PCS studies, we are expecting to improve the understanding for electron correlations and autoionization decay dynamics in this two-electron system.

5.3.1 Partial cross sections

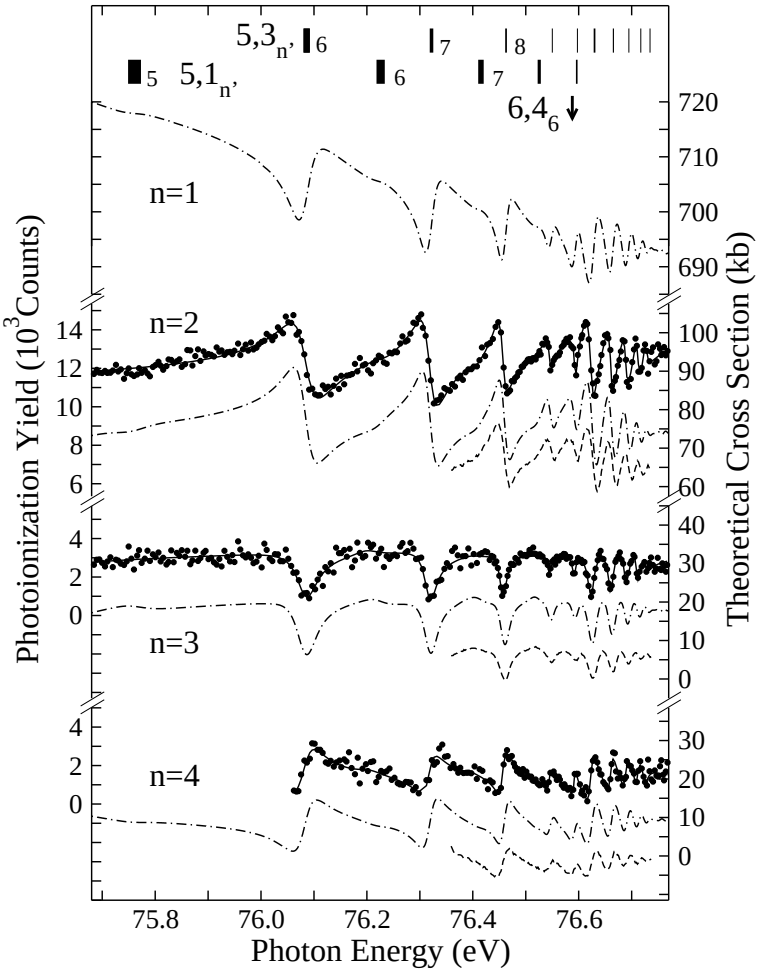

Figure 5.5: Experimental partial cross sections, σ_n^5, leading to the final states $He^+(n)$, with $n = 2$, 3, and 4, along with the results of the eigenchannel R-matrix calculations performed by T. Schneider [33]. The data were taken in the photon-energy region between 75.68 eV and 76.77 eV. The two vertical-bar diagrams in the upper part of the figure give the assignments of the double-excitation resonances by specifying n'; with the widths of bars being proportional to the linewidths of the corresponding resonances [31]. The vertical arrow in the upper right corner marks the calculated energy of the perturber $6, 4_6$. The filled data points are the present experimental results, with the solid curves through the data points representing the fit results. The dashed curves represent the data by Menzel *et al.* [34] and the dash-dotted curves the results of the R-Matrix calculations convoluted with a Gaussian of 6 meV width (FWHM) to simulate finite experimental resolution.

As mentioned before, the Fano formula given in Eq. (3.3), which has been developed for describing the lineshapes of resonances in the TCS, has the same mathematical structure as the exact formula by Starace given in Eq. (3.8) for describing the resonances

in the PCS [59]. As a consequence, it is possible to describe the PCS by the Fano formula, but in this case, q represents only an effective parameter without a deeper physical meaning. In analyzing our data, we fitted the various PCSs for a given energy region by the Fano formula in a parallel least-squares fit procedure using a single Gaussian to simulate the experimental resolution function. In this way, the σ_n leading to different final states of $He^+(n)$ were fitted to Eq. (3.3) with the same experimental resolution Ω, energy position E_r, and linewidth Γ, but different Fano q parameters. The results of this fit procedure are given as solid curves through the data points in Figs. 5.5 to 5.9. The data below the SITs I_5 to I_7 were calibrated at the energy of resonance $5, 3_6$ (76.083 meV) as given by Domke *et al.* [30], and photon energies below the SITs I_8 and I_9 were calibrated to theoretical results [32].

The present experimental data together with theoretical calculations from the eigenchannel R-matrix calculations by Schneider *et al.* [33] and previous measurements by Menzel *et al.* [34] are presented in Figs. 5.5 to 5.9 by the solid points, dash-dotted curves, and dashed curves, respectively. The least-squares-fit results are described by solid lines through the data points in these figures. The results of R-matrix calculations are convoluted with a Gaussian of 6 meV width (FWHM) to simulate experimental resolution; they are given in units of kb on the right ordinate. The basic idea of the R-matrix method has been described in chapter 6.1, and the details for the configurations of the target are in the publication of Schneider *et al.* [33]. Note that, in order to match the experimental data to the theoretical PCSs below the SITs I_6 to I_9, the latter had to be shifted to higher energy by 4 meV, 12 meV, 12 meV, and 10 meV, respectively.

Note that for convenience we employ in our discussion the notation σ_n^N to label the different PCSs. As defined above, the lower index n ($n = 1, 2, 3, ..., N-1$) refers to the principal quantum number of the single electron in the ionized final state, He^+(n). N is the quantum number of the inner electron in the doubly excited states, i.e. the corresponding data are measured below the ionization threshold I_N. Fig. 5.5 displays the results of the present work for the PCSs σ_n^5 (with $n = 2$, 3, and 4). The error bars in the cross sections were estimated in the least-square fit procedures to be $\pm$ 2% for σ_2^5, $\pm$ 10% for σ_3^5, and $\pm$ 15% for σ_4^5. This behavior can be readily understood on the following facts: (i) the lower decay channels have larger cross sections; (ii) the corresponding photoelectrons have higher kinetic energies leading hence to a higher transmission through the TOF spectrometer. Both facts give rise to higher count rates and therefore to smaller error bars. The principal series $5, 3_{n'}$ is observed up to resonance $n' = 15$. The present relative measurements agree well with those of Menzel *et al.* with respect to lineshapes and energy positions of the resonances in all three decay channels. The previously in σ_3^5 and σ_4^5 unobserved resonances $5, 3_6$ and $5, 3_7$ are related to photoelectrons with relatively low kinetic energies, demonstrating the enhanced capability of the TOF analyzers used here in detecting photoelectrons with kinetic energies as low as 350 meV at sufficiently high count rates. In the $n = 2$ channel, the resonances $n' = 6$, 7, and 8 of the secondary series $5, 1_{n'}$ could be detected in the fit analysis with the present monochromator resolution of $\cong$ 6 meV (FWHM).

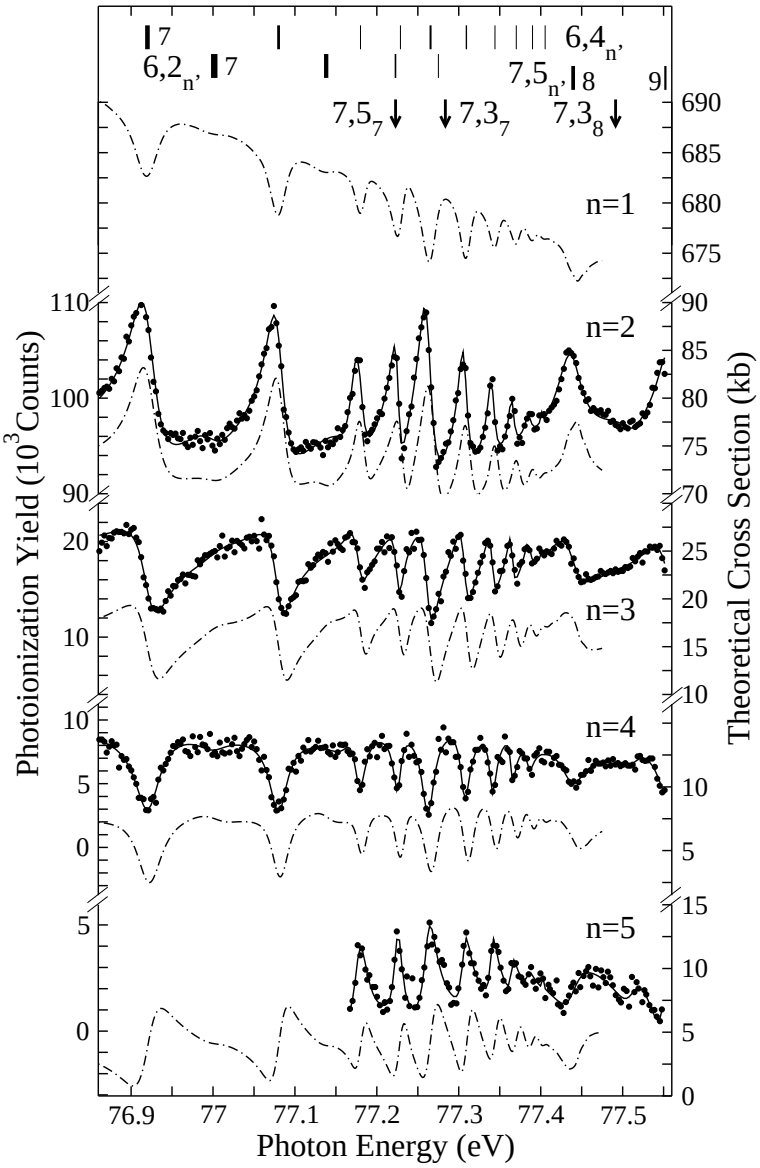

Figure 5.6: Experimental partial cross sections σ_n^6 leading to the final states $He^+(n)$, with $n = 2$, 3, 4, and 5, respectively, in the energy region from 76.85 eV to 77.56 eV, along with the results of the eigenchannel R-matrix calculations; for details, see the caption of Fig. 5.5.

The PCSs below the ionization threshold I_6, with the perturbers $7, 5_8$ and $7, 5_9$, and below the ionization threshold I_7, with the perturber $8, 6_{10}$, are shown in Figs. 5.6 and 5.7, respectively. The principal series $6, 4_{n'}$ and $7, 5_{n'}$ are observed up to the resonances $n' = 16$ and 19, respectively. Note that the resonances $7, 5_{10}$ and $7, 5_{15}$ are almost completely suppressed due to interferences with the perturbers $8, 6_8$ and $8, 6_9$, respectively. These findings agree well with the results of earlier studies of the total photoionization cross sections [30]. The error bars in the PCS curves were estimated to be ± 1% (σ_2^6), ± 1% (σ_2^7), ± 3% (σ_3^6), ± 2% (σ_3^7), ± 6% (σ_4^6), ± 5% (σ_4^7), ± 11% (σ_5^6), and ± 10% (σ_5^7). Again, the resonances $6, 2_7$, $6, 2_8$, and $7, 3_8$ of the secondary series are observed in the fit analysis of σ_2^6 and σ_4^7, respectively. Due to small partial cross sections

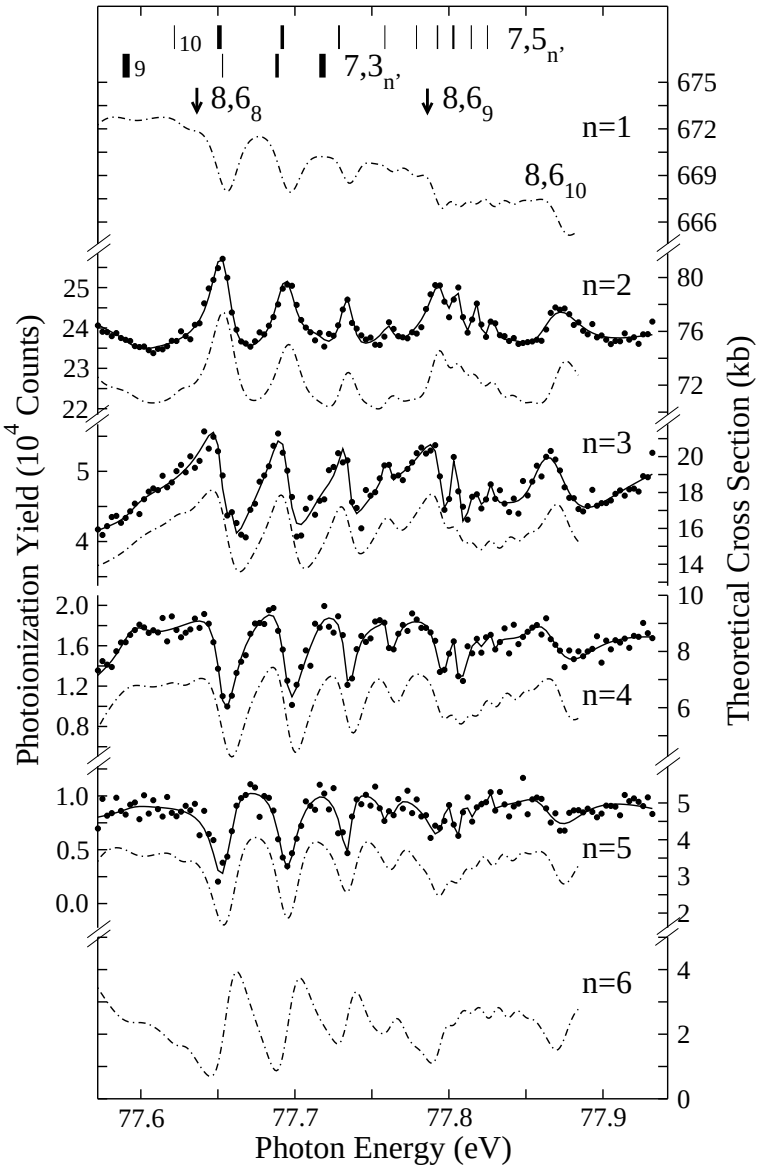

Figure 5.7: Experimental partial cross sections σ_n^7 leading to the final states $He^+(n)$, with n = 2, 3, 4, and 5, respectively, in the energy region from 77.56 eV to 77.92 eV, along with the results of the eigenchannel R-matrix calculations. Note that the plotted theoretical results were shifted by 12 meV to lower energies; for details, see the caption of Fig. 5.5.

and relatively low transmission rate of the TOF spectrometer for slow electrons, the PCS σ_5^6 in the energy region below 77.155 eV (Fig. 5.6) and the PCS σ_6^7 (Fig. 5.7) could not be obtained from the present measurements.

Figures 5.8 and 5.9 display for the first time the experimental PCSs σ_n^8 and σ_n^9 (with $n = 2 - 6$). The energy positions of the perturbers $9, 7_9$, $9, 7_{10}$, $10, 8_{10}$, and $10, 8_{11}$ are also marked in the figures. In general, there is good agreement for the variations in the lineshape, the amplitudes, and the relative positions of the resonances between the experimental and theoretical spectra. Statistical error bars in the PCS curves were estimated to be $\leq \pm$ 1% (σ_2^8 and σ_2^9), $\pm$ 1% (σ_3^8 and σ_3^9), $\pm$ 3% (σ_4^8), $\pm$ 2% (σ_4^9), $\pm$

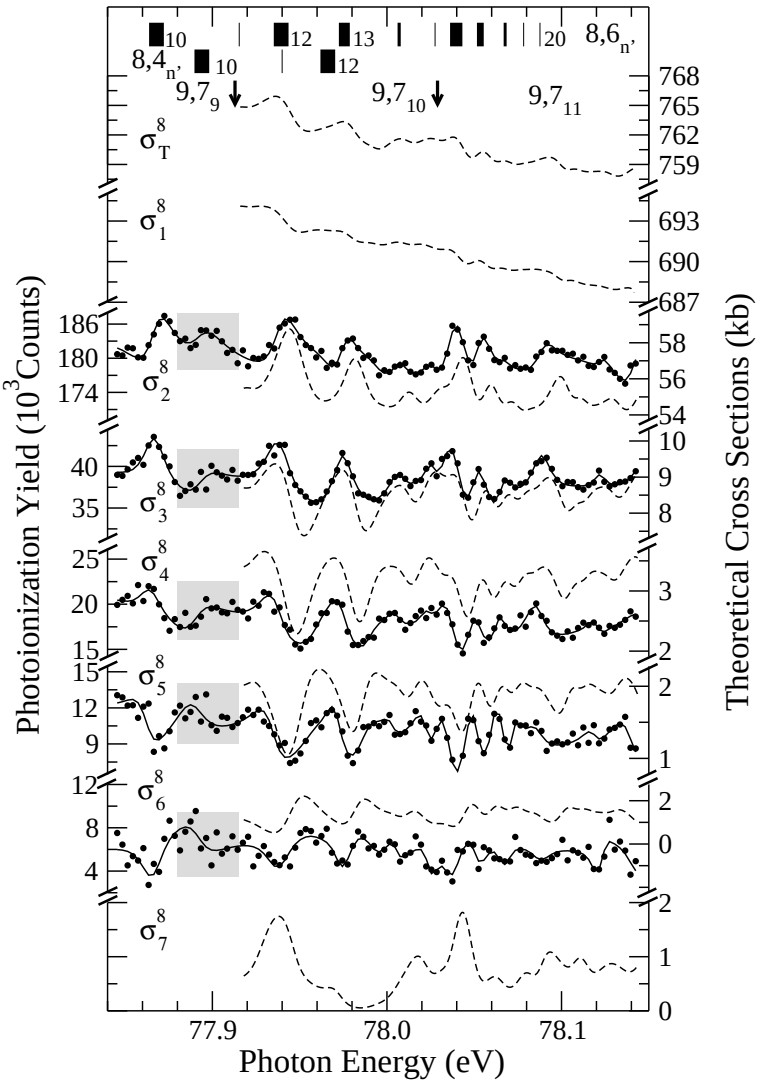

Figure 5.8: Experimental partial cross sections, σ_n^8, leading to the final states $He^+(n)$, with $n = 2-6$, respectively, in the photon-energy region between 77.84 eV and 78.15 eV, along with the results of the eigenchannel R-matrix calculations. The energy position of the resonance $8, 4_{10}$ of the secondary series is marked with grey bars. For details, see the caption of Fig. 5.5.

6% (σ_5^8), ± 4% (σ_5^9), ± 11% (σ_6^8), and ± 7% (σ_6^9). Note that the possible systematic fluctuations caused by normalizing the spectra to σ_1 are not taken into account in these numbers. The increase of the error bar with higher excitation can also be understood by taking into account its lower cross section and correspondingly lower transmission through the TOF spectrometer, which is consistent with the results below the SIT I_7. Due to small PCSs and the relatively low transmission rate of the TOF spectrometer for very slow electrons, the PCSs σ_7^8, σ_7^9, and σ_8^9 could again not be obtained from the present measurements.

Energy position and width of the resonance $8, 4_{10}$ of the secondary series are marked by grey bars in figure 5.8, which is zoomed out together with the resonance $8, 6_{10}$ in figure 5.10. The experimental total cross section [30] in the region was also plotted in

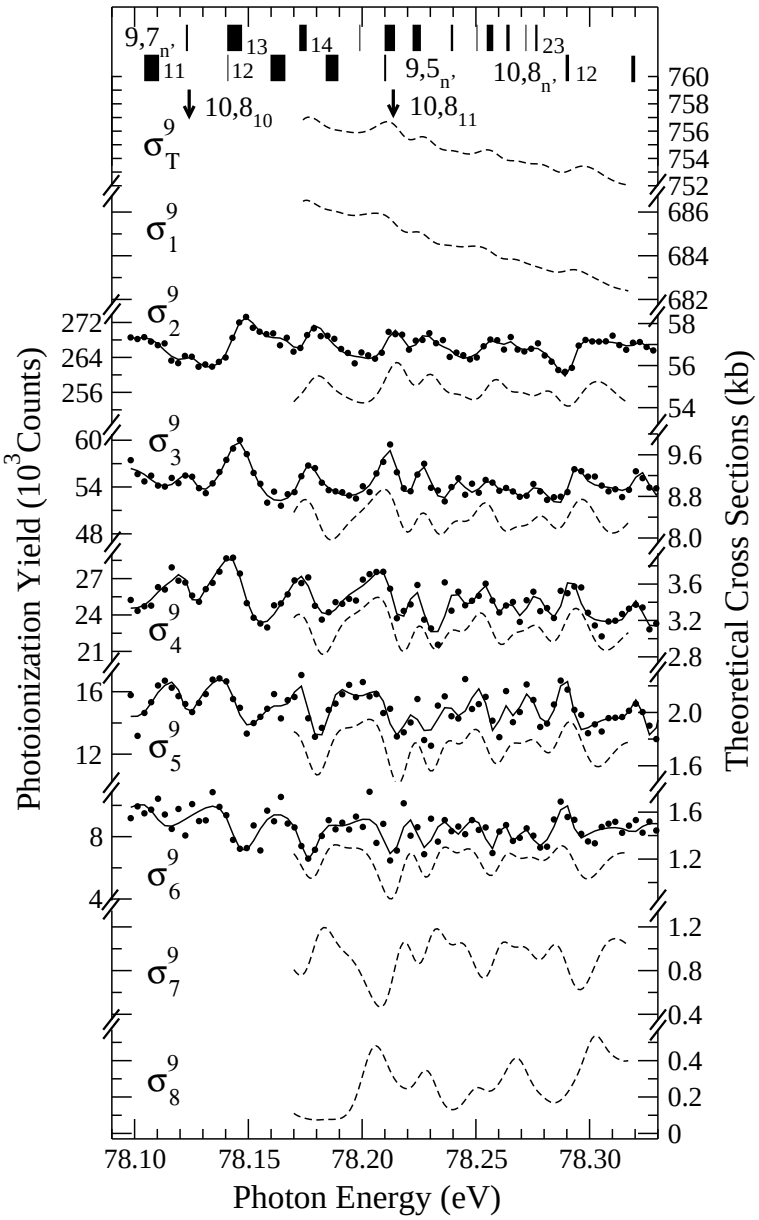

Figure 5.9: Experimental partial cross sections, σ_n^9, leading to the final states $He^+(n)$, with $n = 2-6$, respectively, in the photon-energy region between 77.84 eV and 78.15 eV. For details, see the caption of Fig. 5.5.

this figure. Interestingly, although the TCS displays good statistics and high resolution, $\cong$ 4 meV for TCS and $\cong$ 6 meV for PCS, the resonance $8, 4_{10}$ is observed clearly in all decay channels below the SIT I_8 in contrast to its absence in the TCS, which could be completely suppressed due to interferences with the perturbers. This is due to the fact that the resonance $8, 4_{10}$ shows quite different lineshapes in the partial cross sections which cancel out in the TCS. These different lineshapes are due to different coupling to various σ_n. In figure 5.10(f), the signal-to-noise ration is therefore very low, which traces of the resonance $8, 4_{10}$ can only be identified by the fit curve. The present PCS measurements below the SITs I_7 and I_9 were published in Refs. [37] and [104].

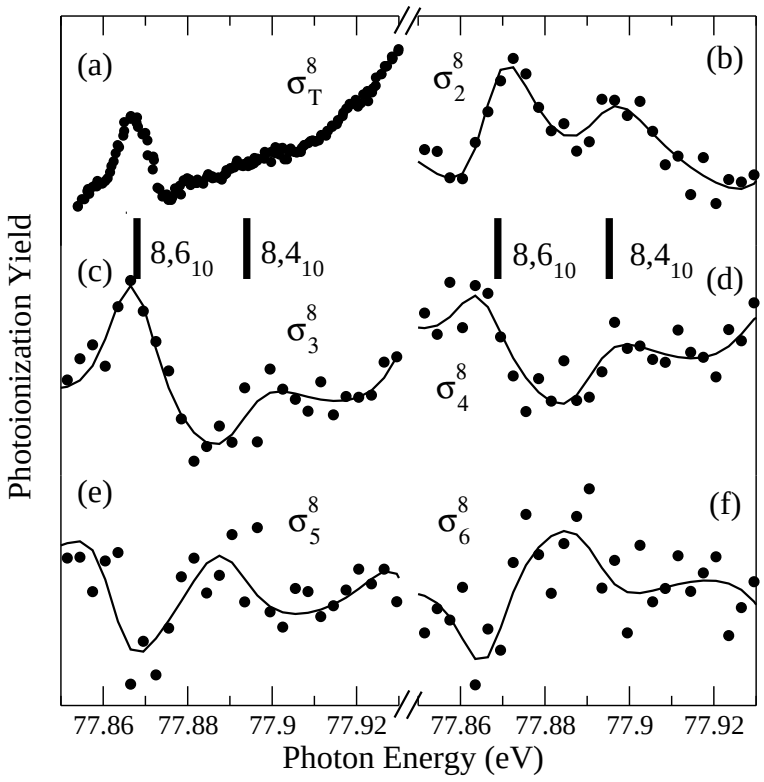

Figure 5.10: Experimental partial cross sections σ_n^8 for resonances $8, 6_{10}$ and $8, 4_{10}$ in the energy region from 77.85 eV to 77.93 eV.(a) for previous total cross section [30], (b) for σ_2^8, (c) for σ_3^8, (d) for σ_4^8, (e) for σ_5^8, and (f) for σ_6^8. For details see figure 5.5.

5.3.2 General pattern

In 1995, Menzel *et al.* [35] found from their experimental PCSs for doubly excited helium below the SIT I_5 that the resonances below different ionization thresholds exhibit similar variations when $N - n$ is of the same value; this observation is called 'general pattern'. Later, these patterns in the PCSs were discussed theoretically up to the SIT I_9 by Schneider *et al.* [33] and van der Hart *et al.* [63]. With propensity rules that can be derived from the molecular adiabatic approximation introduced in Sect. 3.2.1, Schneider *et al.* [33] were able to understand these general patterns in the PCSs very well. In the present work, we shall confirm these general patterns experimentally and discuss them on the basis of the propensity rules.

As we discussed before in Sect. 3.2.1, the adiabatic avoided-crossing potential curves can be identified by the approximate quantum numbers $[n_\lambda n_\mu m]$ in a molecular picture. The mechanism of autoionization relies on the nonadiabatic transitions between these adiabatic avoided-crossing potential curves, in full analogy to electronic transition in molecules. *Radial* transition are sensitive to the change of the wave function as a function of R, i.e. via the change of n_μ. Therefore, these transitions occur preferentially through an avoided-crossing of two potential curves. The second kind of non-adiabatic transitions due to *rotational* coupling, the change of m between potential curves. Finally, there is no explicit mechanism to change n_λ. Hence, decays with $\Delta n_\lambda \neq 0$ are strongly suppressed.

In this way, three propensity rules for the autoionization process can be derived. The different propensity rules caused by different decay mechanisms are given in the order of the efficiency of the underlying decay mechanism [31, 33]:

$$\begin{array}{ll} (A) & \text{reduction of } [n_\mu/2] \\ (B) & \text{change of } m \\ (C) & \text{reduction of } n_\lambda. \end{array} \tag{5.1}$$

The propensity rules (A), (B), and (C) of Eq. (5.1) group the $^1P^o$ resonant states of helium into three classes I-III with typical widths separated by at least two orders of magnitude, $\Gamma_I : \Gamma_{II} : \Gamma_{III} \approx 10^4 : 10^2 : 1$. According to Eq. (3.19), the two classification schemes $[n_\lambda n_\mu m]_{n'}$ and $N, K_{n'}$ are equivalent. Therefore, the propensity rules (A) given in expression (5.1) can be transformed into "reduction of N". One can apply the approximate quantum numbers $N, K_{n'}$ to describe not only bound states but also continuum states. Thus for the principal Rydberg series $K = N - 2$, the decay from bound states N, K to continuum states n, k can occur via the propensity rule (A) by $\Delta N = N - n = \Delta K = K - k = 1, 2, ...$ The differences in the efficiency of the decay mechanisms are so strong that a decay via rule (B) or (C) shows only visible influence on the spectra if the decay processes on the basis of the preceding propensity rule (A) are not possible [31, 33]. The coupling matrix elements, which lead to the propensity rules, are essentially very similar to the matrix elements that are relevant for the resonance parameters [106]. We can, therefore, conclude that resonances, which decay via the same propensity rule and have the same change in nodal structure, show similar lineshapes. In particular, most of the spectral features in doubly excited helium are governed by propensity rule (A). In this case, we expect similar lineshapes for the resonances in different PCSs if the decay leads to the same change in ΔN and ΔK, i.e. the changes of the nodal structure in the radial wave functions are identical. For example, propensity rule (A) results in the expectation that the principal series in the PCS σ_4^6 exhibits the same resonance profile as that in the PCS σ_3^5. This expectation was confirmed by Menzel *et al.* [35] for resonances up to the ionization thresholds I_5.

Fig. 5.11 presents examples of such cross section patterns, namely σ_2^4, σ_3^5, σ_4^6, and σ_5^7; in these PCSs, the resonances of the principal series decay by $\Delta N = N - n = 2$. In order to demonstrate the 'general patterns', the photon energies were scaled to the effective quantum numbers μ_N by the Rydberg formula given in Eq. (4.2). The similarities of the cross section curves are evident except for the energy regions of perturber states indicated by vertical arrows. As mentioned above, the perturber states affect the resonance energies and linewidths of the various resonances and, as a consequence, the regularities fade out in the vicinity of perturber states, but further away, the 'general pattern' is restored. In the present measurements below the ionization threshold I_9, similar general patterns were observed in σ_4^5 and σ_5^6, with $\Delta N = 1$, in σ_2^5, σ_3^6, σ_4^7 and σ_5^8 with $\Delta N = 3$ in σ_2^6, σ_3^7, σ_4^8, and σ_5^9 with $\Delta N_2 = 4$, σ_2^7, σ_3^8, and σ_4^9 with $\Delta N = 5$, as well as σ_2^8 and σ_3^9 with $\Delta N = 6$. However, in the energy region of the higher ionization thresholds, such as in the SITs

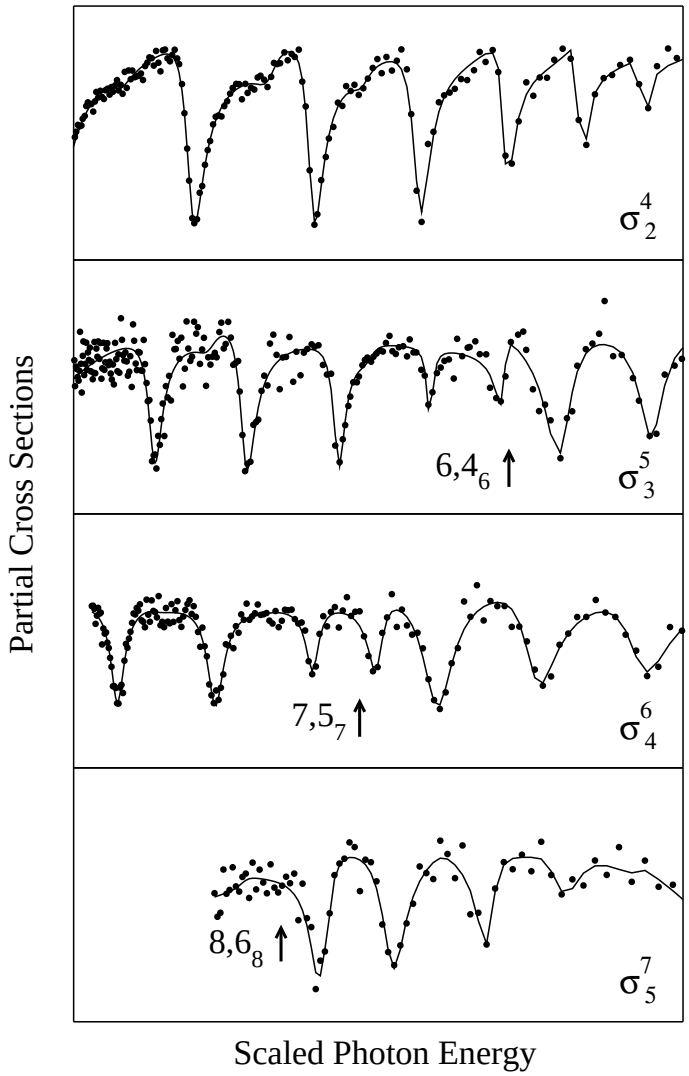

Figure 5.11: Partial photoionization cross sections σ_n^N as a function of scaled photon energy. For details see figure 5.5.

I_8 and I_9, the general patterns become very weak due to the complex structures caused by interferences with two additional perturber states that interact with the principal Rydberg series.

5.3.3 Mirroring behavior

The TCS consists of a number of PCSs, which are defined by the quantum numbers of the outgoing electron and the remaining ion. After dividing the PCSs in any two groups P and Q, experimental and theoretical studies found that the variations in the vicinity of a resonance between the PCSs P and Q showed a similar variation [33, 36, 37, 38, 104]. This was called 'mirroring behavior' by Liu and Starace [36, 38], who first discussed it with an analytical expression for approximate conditions. Here, the energy axis is taken as the mirroring plane. These authors assume that this analytical expression can be used to understand mirroring behavior for any general case, not only in photoionization

process but also in photodetachment of negative ions [36, 38]. However, this explanation does not work for doubly excited helium.

If the TCS is regarded as the sum of two random groups of PCSs, denoted by P and Q, the PCS P can be expressed by Eq. (3.7), and for the PCS Q the same formula with P replaced by Q can be used. Note that the PCS P and the PCS Q can be individual PCSs or the sum of a number of individual PCS, which in the present case are the σ_n. By using Starace formula [59] which establishes relations between the parameters ρ and σ_T^0 in the Fano formula given in Eq. (3.6) for the TCS and the parameters σ_P^0, σ_Q^0, and α used in Eq. (3.7), namely,

$$\begin{aligned}
\sigma_P^0\langle|\alpha|^2\rangle_P + \sigma_Q^0\langle|\alpha|^2\rangle_Q &= \rho^2\sigma_T^0, &(5.2)\\
\sigma_P^0\mathrm{Re}\langle\alpha\rangle_P + \sigma_Q^0\mathrm{Re}\langle\alpha\rangle_Q &= \rho^2\sigma_T^0, &(5.3)\\
\sigma_P^0\mathrm{Im}\langle\alpha\rangle_P - \sigma_Q^0\mathrm{Re}\langle\alpha\rangle_Q &= 0, &(5.4)
\end{aligned}$$

Liu and Starace derived the PCS σ_Q [36]

$$\begin{aligned}
\sigma_Q &= \sigma_Q^0 - \frac{\sigma_P^0}{1+\epsilon^2}\{2\epsilon q\mathrm{Re}\langle\alpha\rangle_P - 2q\mathrm{Im}\langle\alpha\rangle_P + q^2\langle|\alpha|^2\rangle_P\}\\
&\quad + \frac{q^2\rho^2\sigma_T^0}{1+\epsilon^2}, \qquad (5.5)
\end{aligned}$$

with the approximation $q\rho^2 \to 0$ when $\rho^2 \to 0$, but with $q^2\rho^2$ remaining finite. This has been shown by Nora Berrah and coworkers for two resonances of doubly excited Ar that are extremely weak in the TCS; in the PCSs, however, the resonances are clearly visible [107]. Although $\rho^2 \to 0$ is required for a mirroring behavior to occur, it has been observed in the theoretical photoionization cross section of Li^- even for ρ^2 as high as 0.3 [36]. In contrast to this, two sets of PCSs for helium in the double excitation region do not always mirror each other even for $\rho^2 \cong 0.001$ (see theoretical part in the dissertation), which can be understood well with a more general expression without any approximations

$$\begin{aligned}
\sigma_Q &= \frac{\sigma_Q^0}{1+\epsilon^2}\{\epsilon^2 + 2\epsilon(q\mathrm{Re}\langle\alpha\rangle_Q - \mathrm{Im}\langle\alpha\rangle_Q)\\
&\quad + (1 - 2q\mathrm{Im}\langle\alpha\rangle_Q - 2\mathrm{Re}\langle\alpha\rangle_Q + (q^2+1)\langle|\alpha|^2\rangle_Q)\}\\
&= \sigma_Q^0 + \frac{\sigma_Q^0}{1+\epsilon^2}\{2\epsilon(q\mathrm{Re}\langle\alpha\rangle_Q - \mathrm{Im}\langle\alpha\rangle_Q)\\
&\quad + (-2q\mathrm{Im}\langle\alpha\rangle_Q - 2\mathrm{Re}\langle\alpha\rangle_Q + (q^2+1)\langle|\alpha|^2\rangle_Q)\}\\
&= \sigma_Q^0 + \frac{\sigma_P^0}{1+\epsilon^2}\{2\epsilon(-q\mathrm{Re}\langle\alpha\rangle_P + \mathrm{Im}\langle\alpha\rangle_P + q\rho^2\sigma_T^0/\sigma_P^0) + (2q\mathrm{Im}\langle\alpha\rangle_P\\
&\quad + 2\mathrm{Re}\langle\alpha\rangle_P - 2\rho^2\sigma_T^0/\sigma_P^0 - (q^2+1)\langle|\alpha|^2\rangle_P) + (q^2+1)\rho^2\sigma_T^0/\sigma_P^0\}\\
&= \sigma_Q^0 - \frac{\sigma_P^0}{1+\epsilon^2}\{2\epsilon(q\mathrm{Re}\langle\alpha\rangle_P - \mathrm{Im}\langle\alpha\rangle_P)\\
&\quad - 2q\mathrm{Im}\langle\alpha\rangle_P - 2\mathrm{Re}\langle\alpha\rangle_P + (q^2+1)\langle|\alpha|^2\rangle_P\}\\
&\quad + \frac{2q\rho^2\sigma_T^0}{1+\epsilon^2}\epsilon + \frac{q^2\rho^2\sigma_T^0}{1+\epsilon^2} - \frac{\rho^2\sigma_T^0}{1+\epsilon^2}. \qquad (5.6)
\end{aligned}$$

Comparing Eq. (3.7) with Eqs. (5.5) and (5.6), one can realize that the second term plays a key role for the mirroring on the lineshape of the resonance between σ_P and σ_Q. *The last three terms described the Fano-like variation of the resonances in the TCS determine whether the resonances in the PCS P and PCS Q exhibit a mirroring behavior.* The resonances in the two groups P and Q of the PCSs mirror each other if the second term of Eq. (5.6) is dominant as compared to the last three terms. If $|q| >> 1$ and $\rho^2 \rightarrow 0$, the third and fifth terms in Eq. (5.6) can be neglected in comparison with the fourth term. In this case, Eq. (5.6) results in Eq. (5.5) if one omits, in addition to the third and fifth term, all contributions of the second term that do not include q or q^2. As discussed in Ref. [36], in this case the resonances display a Lorentzian profile in the TCS.

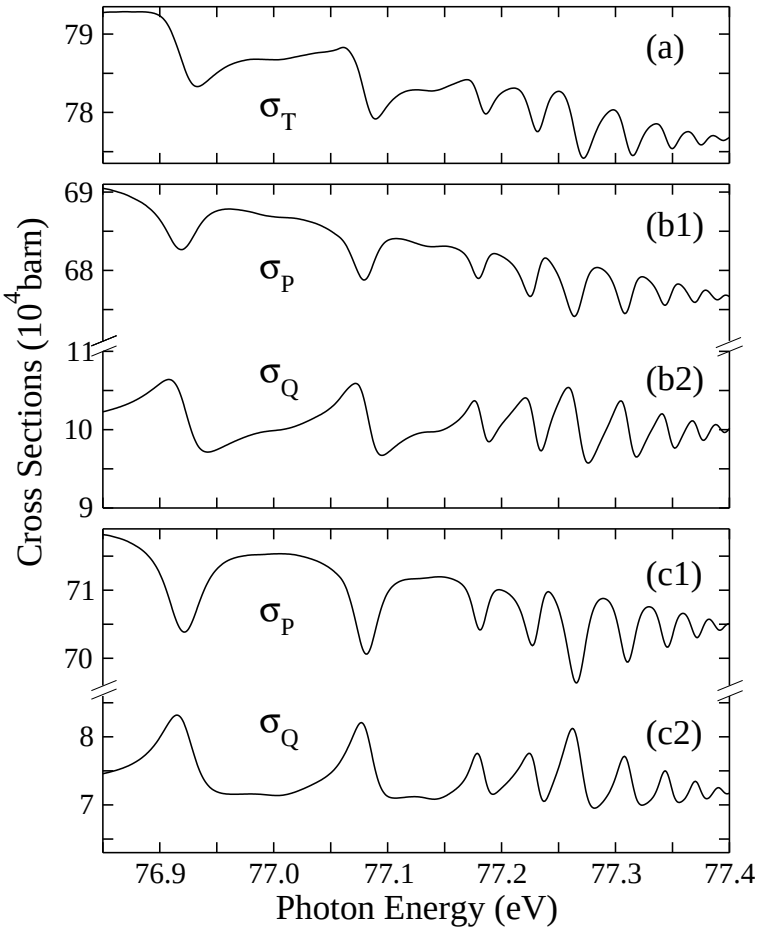

Figure 5.12: Cross sections below the ionization threshold I_6 obtained from eigenchannel R-matrix calculations [33] and convoluted with a Gaussian resolution function of 6 meV width (FWHM). (a) Total cross section σ_T. In (b) and (c) the PCS σ_P and σ_Q were established in different ways: (b1) $\sigma_P = \sigma_1$ and (b2) $\sigma_Q = \sigma_2 + \sigma_3 + \sigma_4 + \sigma_5$; (c1) $\sigma_P = \sigma_1 + \sigma_3 + \sigma_4 + \sigma_5$ and (c2) $\sigma_Q = \sigma_2$.

In the region between the SITs I_5 and I_7 of He^+, the Fano parameter ρ^2 is of the order of 0.01 for the principal series (see Fig. 5.12 (a) for the theoretical TCS below I_6 [33]). In the other tablets of Figs. 5.12, we plot two examples, with the TCS $\sigma_T = \sigma_P + \sigma_Q$ being

separated into two groups. In the first example $\sigma_P = \sigma_1$ and $\sigma_Q = \sigma_2 + \sigma_3 + \sigma_4 + \sigma_5$ (b1, b2); in the second example, $\sigma_P = \sigma_2$ and $\sigma_Q = \sigma_1 + \sigma_3 + \sigma_4 + \sigma_5$ (c1, c2). In the second example, the PCS σ_P mirrors the PCS σ_Q very well [Figs. 5.12 (c1) and (c2)]. In contrast to this, the mirroring behavior is not well expressed in the first example [Fig. 5.12 (b1) and (b2)]. This can be understood as follows: A mirroring behavior is expected if the amplitudes of the resonances in the TCS are small compared to variations in the PCS, i.e. if terms three to five in Eq. (5.6) are small compared to term two. In helium, however, each single PCS σ_n exhibits amplitudes that are of the same order of magnitude as in σ_T. Since this holds for all ionization thresholds I_N up to $N = 9$ (see Fig. 3 in Ref. [33]), no general mirroring behavior will be expected in the double-excitation region of helium. Mirroring behavior occurs only accidentally, namely if the PCS σ_P already mirrors σ_T [see Fig. 6 (a) and (c1)]. In this cases, the second term in Eq. (5.6) mimics σ_T and a mirroring behavior is observed. Even in cases where σ_P is established by a number of σ_n, no general mirroring behavior is expected since the amplitude of the variation in σ_P will still not be large as compared to the variation in σ_T. In summary, for the existence of a general mirroring behavior the condition $\rho^2 \to 0$ is not sufficient. In addition to this it is also necessary that the amplitudes of resonances in the PCS are considerably larger than those in the TCS. However, as observed in the theoretical cross sections up to ionization threshold I_9 [33], the amplitudes in the PCS decrease by the same amount with increasing N as the amplitudes in the TCS. As a consequence, we do not expect a general mirroring behavior in helium below higher-N ionization thresholds I_N with ρ^2 even much smaller than 0.01. This conclusion will be further confirmed by the studies of the secondary and third Rydberg series below the SITs I_4 in the theoretical part of this dissertation.

Since the sum of any two PCSs can be expressed mathematically by the Fano formula, the analysis given above can also be employed to discuss and understand the mirroring behavior of any two individual PCSs although the sum of these will not be the TCS, such as in case of σ_2^6 and σ_4^6 as well as σ_3^6 and σ_5^6 (see Fig. 5.6). In these cases, the resonances in $\sigma_S = \sigma_2^6 + \sigma_4^6$ and $\sigma_S = \sigma_3^6 + \sigma_5^6$ are almost canceled out, and the σ_S are expected to be quite structureless. On the other hand, if any σ_S shows considerable structure, the contributing individual partial cross sections do not show mirroring behavior. In addition, the perturbers have no effect on the mirroring behavior between the PCS P and PCS Q. In addition, it should be noted that below the SITs I_5 to I_7, the PCS σ_2^N mirrors the PCS σ_4^N and the PCS σ_3^N mirrors the PCS σ_5^N (not for $N = 5$). This behavior might be due to a relation between the propensity rules and the mirroring behavior and can be an interesting topic for future studies.

5.4 Angle-resolved measurements up to I_7

The ADP, β_n, and the PCS, σ_n, show different dependences on the dipole matrix element for excitation and the Coulomb matrix element for decay as well as on the phase shifts of various outgoing channels. Therefore, resonances can be clearly seen in the ADP, β_n, but

not in the PCS, σ_n, or vice versa. Consequently, the ADP can be used for an additional check on theoretical models, and one expects that additional resonances are resolved from the ADP. From the point of view of complete measurements, the ADP measurements are also necessary for a complete check on quantum mechanics.

5.4.1 Differential cross sections and β parameter

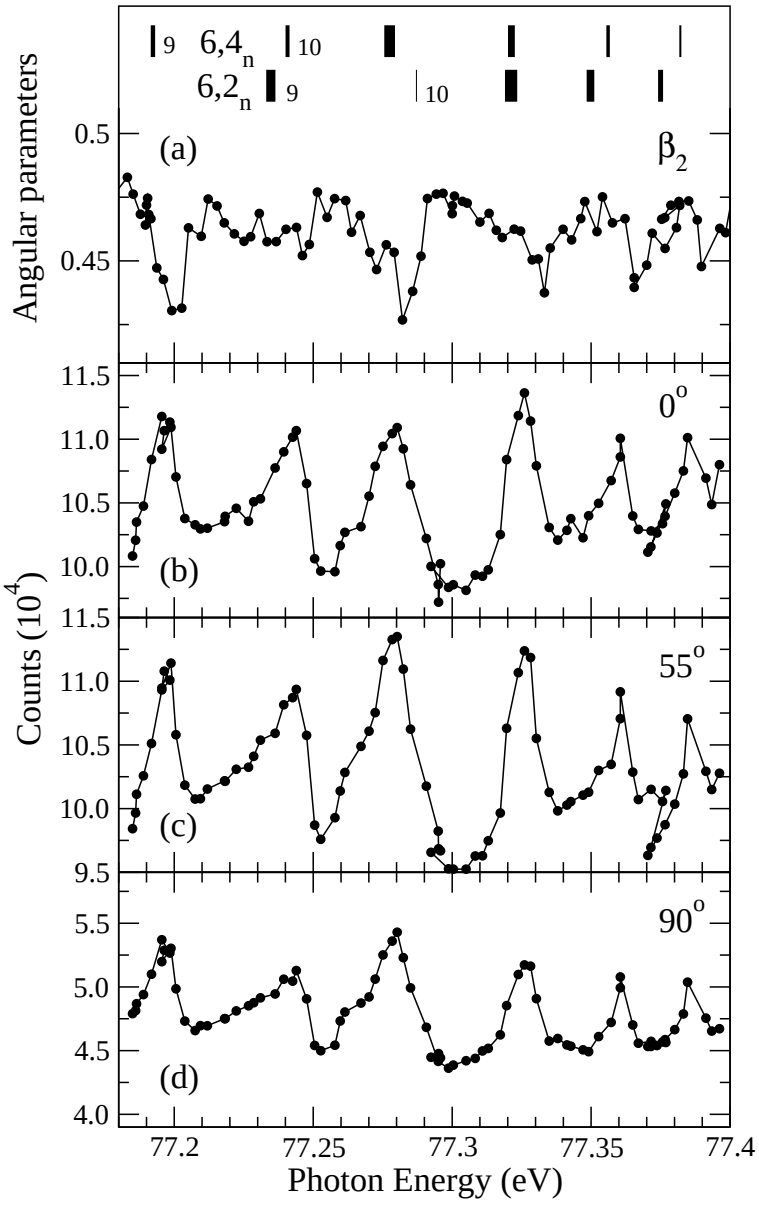

Figure 5.13: Differential cross sections, $d\sigma_2/d\Omega$, measured at angles (b) 0°, (c) 55°, and (d) 90° below the SIT I_6 and (a) corresponding angular distribution parameter β_2^6. Solid points represent the present experimental results and solid lines though the data points serve as the guides to the eye. The two vertical-bar diagrams in the upper part of the figure give the assignments of the double-excitation resonances specified by n', with the widths of bars being proportional to the linewidths of the corresponding resonances [31].

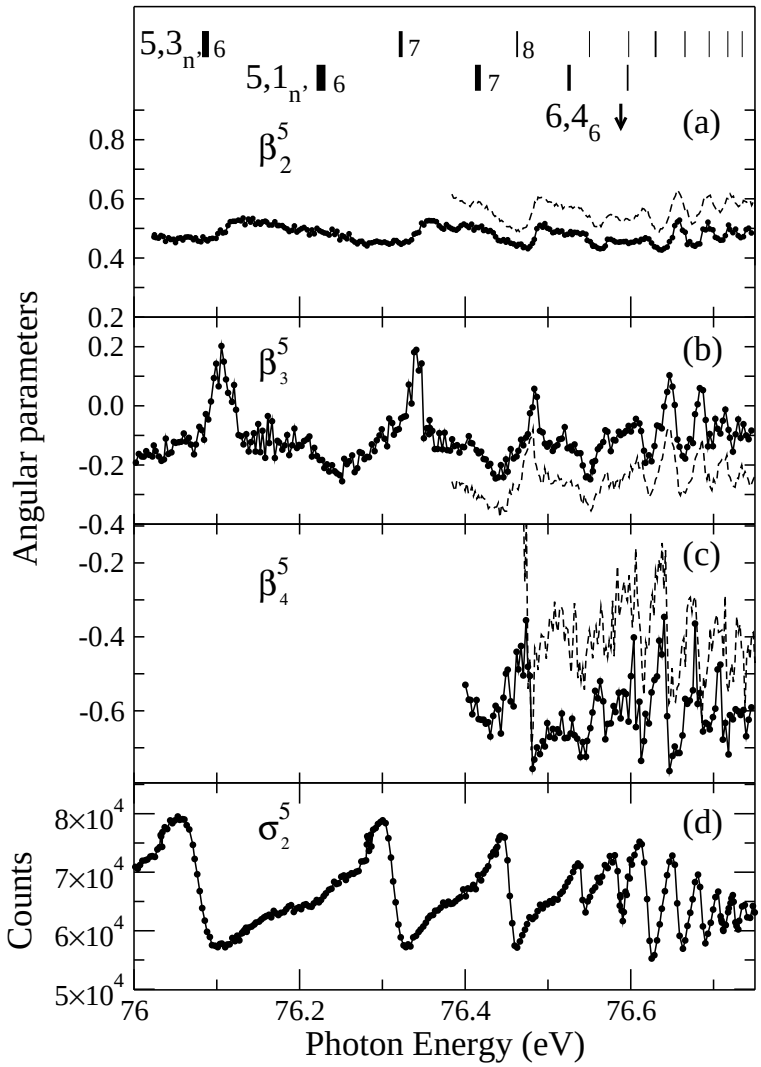

Figure 5.14: Angular distribution parameters β_n^5 with (a) $n = 2$, (b) $n = 3$, and (c) $n = 4$, respectively, together with (d) the PCS σ_2^5 below the SIT I_5; the measurements of Menzel *et al.* were displayed by dash lines. For details see Fig. 5.13.

As an example, the differential cross sections (DCS) ,$d\sigma_2/d\Omega$, measured at angles 0°, 55°, and 90° below the SIT I_6 are presented in Fig. 5.13(b), (c), and (d) together with the corresponding ADP β_2^6 in Fig. 5.13(a). The solid points represent the measurements and the solid lines are a guide to the eyes. In general, the resonances cause quite similar variations in the DCS, i.e. only slight differences were found in Fig. 5.13(b)-(d). Note that the same scale was used on the ordinate in this figure. The $d\sigma_2/d\Omega$ taken at 55° exhibits the strongest variations caused by the resonance, but the direct ionization cross section which causes the constant background is almost identical to that at 0°. The direct ionization cross section at 90° is by a factor 2 smaller than those at the other two angles. This is due to the positive mean value of the ADP $\beta_2^6 = 0.47$; its angular distribution of intensity is shown in Fig. 1.1. Indeed, the variations caused by the resonances and its absolute value of β are quite sensitive to those in the DCSs, $d\sigma_2/d\Omega$. The resonance structures seem quite pronounced in $d\sigma_2/d\Omega$, but sometimes they can lead to quite weak

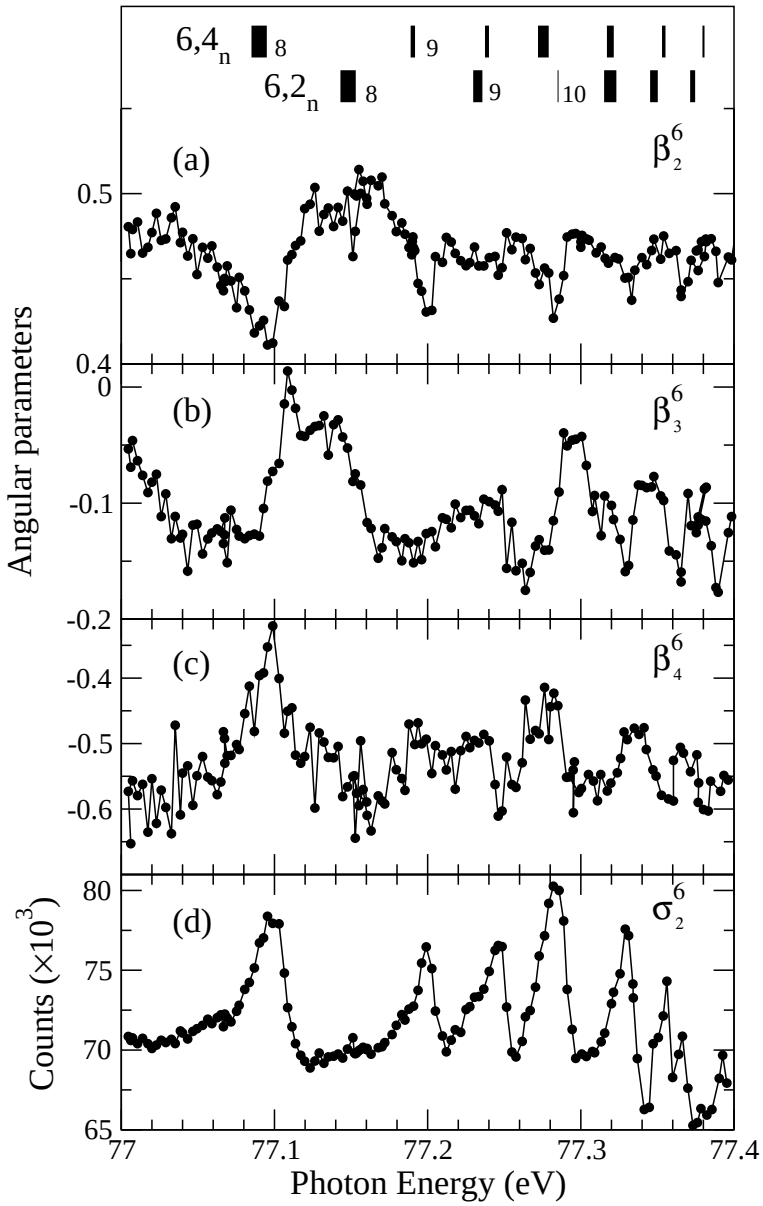

Figure 5.15: Angular distribution parameters β_n^6 with (a) $n = 2$, (b) $n = 3$, and (c) $n = 4$, respectively, together with (d) the PCS σ_2^5 below the SIT I_6; for details see Fig. 5.13.

variations in β. This is also the reason why more TOF spectrometers are needed in the experiments to improve the precision of the measurement.

The results of preliminary measurements of the β parameters below the SITs I_5 to I_7 are presented given in Figs. 5.14, 5.15, and 5.16. For a better identification of the resonances, the present PCSs σ_2^N are also plotted in these figures. Our measurements below the SIT I_5 agree well with the experimental results of Menzel *et al.* [35]. The first two members $5, 3_6$ and $5, 3_7$ of the principal series below the SIT I_5 were observed in the β_2^5 and β_3^5 curves for the first time. These resonances could not be observed in β_4^5 due to the low cross section in combination with a low transmission rate for this slow electrons. Systematic errors could result in large fluctuations of the absolute values of

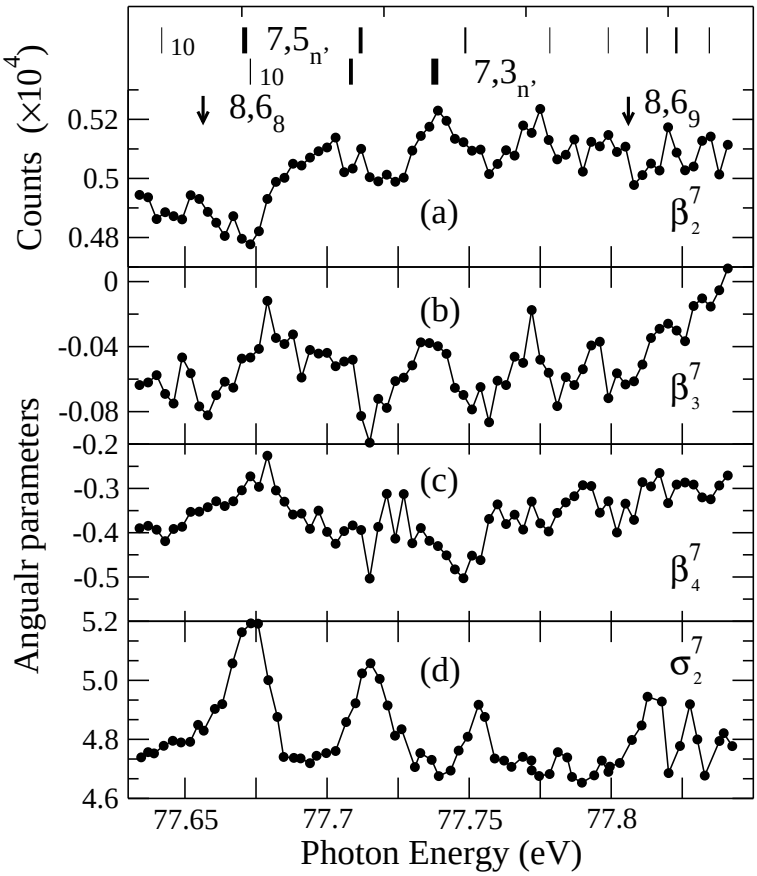

Figure 5.16: Angular distribution parameters β_n^7 with (a) $n = 2$, (b) $n = 3$, and (c) $n = 4$, respectively, together with (d) the PCS σ_2^7 below the SIT I_7; for details see Fig. 5.13.

β as mentioned before. The error bars for the absolute value of β can easily reach more than 50% if only two TOFs are employed. For the results presented in Figs. 5.14, 5.15, and 5.16, three or four TOFs were employed, and the error bars on absolute value of β are estimated to be less than 15%. Considering these error bars, the present absolute values of β^5 are in agreement with previous measurements and calculations published in Ref. [35].

For β^6 and β^7, presented in Figs. 5.15 and 5.16, neither experimental nor theoretical results are available in the literature for comparison. Interestingly, the variations of the resonance $6, 2_8$ are clearly observed in β_2^6 and β_3^6 for the first time. In contrast to the variations in β, resonance $6, 2_8$ is strongly suppressed in σ_2 as shown in Fig. 5.15(d), as well as in the experimental and theoretical PCSs σ_n presented in Fig. 5.6. This can be understood by the different dependences of β and σ on the matrix elements for excitation and decay of the autoionization states as well as on the phase shifts of the various outgoing channels.

In oder to improve the signal-to-noise ratio, the regions below the SITs I_6 to I_7 was again studied in our with 12 TOFs mounted at various angles in the dipole plane. These data are expected to have better statistics and higher transmission rate. However, they are not fully analyzed so far and, therefore, cannot be presented in this dissertation.